Journal of Computational Science 31 (2019) 137–150

Contents lists available at ScienceDirect

Journal of Computational Science

journal homepage: www.elsevier.com/locate/jocs

Uncertainty quantification of computational coronary stenosis assessment and model based mitigation of image resolution limitations

Jacob Sturdy*, Johannes Kløve Kjernlie, Hallvard Moian Nydal, Vinzenz G. Eck, Leif R. Hellevik

Department of Structural Engineering, Norwegian University of Science and Technology (NTNU), Richard Birkelandsvei 1a, 7491 Trondheim, Norway

ARTICLE INFO

Article history:
Received 12 November 2018
Accepted 19 January 2019
Available online 2 February 2019

Keywords:
Coronary stenosis
Uncertainty quantification
Sensitivity analysis
Fractional flow reserve
Hemodynamics
Modeling

ABSTRACT

Coronary artery disease is one of the leading causes of death globally. The hallmark of this disease is the occurrence of stenosed coronary arteries which reduce blood flow to the myocardium. Severely stenosed arteries can be treated if detected, but the diagnostic procedure to assess fractional flow reserve (FFR), a quantitative measure of stenosis severity, is invasive, burdensome to the patient, and costly. Recent computational approaches estimate the severity of stenoses from simulations of coronary blood flow based on CT imagery. These methods allow for diagnosis to be made noninvasively and using fewer hospital resources; however, the predictions depend on uncertain input data and model parameters due to technical limitations and patient variability. To assess the consequences of boundary condition and input uncertainty on predictions of FFR, we developed a model of coronary blood flow. We performed uncertainty quantification and sensitivity analysis of the predictions based on uncertainties in boundary conditions, parameters, and geometric measurements. Our results identified three influential sources of uncertainty: geometric data, cardiac output, and coronary resistance during hyperemia. Further, uncertainty about the geometry of the stenosed coronary branch influences estimates much more than other geometrical data. Limitations of medical imaging contribute uncertainty to predictions as vessels below a certain threshold remain unobserved. We assessed the effects of unobserved vessels by comparing predictions based on both high and low resolution data. Moreover, we introduced a novel method that estimates flow distribution while accounting for unobserved vessels. This method improved FFR predictions in the cases considered by 50% on average.

1. Introduction

Cardiovascular diseases (CVDs) account for more than 17 million deaths each year globally, a number expected to grow to 23.6 million by 2030 [1]. The World Health Organization estimates that coronary artery disease (CAD) caused 7.4 million deaths worldwide (the largest single cause of death) in 2012 [2]. In addition to the social and personal costs of CVDs, the epidemic's economic costs are growing rapidly. In the US, CVDs are projected to triple from 273 billion USD to 818 billion USD from 2010 to 2030 [3]. Coronary artery disease (CAD) leading to myocardial ischemia composes the largest portion of these. CAD describes a buildup of plaques in arterial walls reducing the lumen area of blood vessels, effectively resulting in a narrowing of the blood vessel referred to as a stenosis. The stenosis increases work required to perfuse the myocardial tissue and increases the risk of a clot blocking the artery and leading to an infarction. Given the prevalence and risks of CAD, significant efforts have been made to improve the diagnosis and treatment of this condition by identifying which stenoses are significant and intervening, typically by insertion of vascular stent, to ensure sufficient blood flow through to the myocardium. Diagnosis often occurs only after an individual has noticed the symptoms of CAD- chest pain or in more serious cases heart attack or arrhythmia. Methods to evaluate the significance of a stenosis range from non-invasive imaging based approaches to invasive measurement of blood pressures. If a stenosis is deemed significant, then the patient typically undergoes coronary angioplasty (percutaneous coronary intervention (PCI)) to open the artery and, if deemed beneficial, to insert a stent.

* Corresponding author.
E-mail address: jacob.t.sturdy@ntnu.no (J. Sturdy).

https://doi.org/10.1016/j.jocs.2019.01.004
1877-7503/

The most widely used method of identifying and assessing stenosis severity considers only the visual appearance of the stenosis imaged through coronary angiography via cardiac catheterization. In 2010 more than 1 million cardiac catheterizations were performed in the US [4]. A more objective but invasive method is based on fractional flow reserve (FFR), which is defined as the ratio of maximal blood flow through the stenosed artery to the maximal blood flow through the same artery if the stenosis were not present. FFR may be estimated as the ratio between the pressure distal and proximal to the stenosis measured invasively via pressure wires [5]. De Bruyne et al. [6] found that FFR was independent of the hemodynamic state of the person showing that the measure may perform across a variety of physiological conditions. Additionally, numerous studies show the diagnostic accuracy of FFR (greater than 90%) and associated benefits of improved treatment outcomes and reduced costs [7–9]. Despite these benefits, FFR is typically measured only when operators are uncertain about angiography based assessment of the stenosis [10]. Hannawi et al. also found that nearly three-fourths of physicians surveyed use FFR in less than one-third of cases. Many physicians (47%) reported that the procedure was not available at their institutions, while another significant portion (25%) claimed the time required to set up the test discouraged broader usage. Morris et al. [11] note that FFR is measured in less than 10% of individuals who undergo PCI for CAD in the UK and claim many operators believe their own judgment based on image data and noninvasive testing is sufficient despite evidence to the contrary. Failure to employ FFR more broadly likely results in unnecessary PCI for some while significant stenoses go undiagnosed in others.

Methods that estimate FFR noninvasively may improve diagnosis and treatment of CAD by making quantitative evaluation of CAD severity accessible to a wider number of patients and physicians. Computational fluid dynamics (CFD) may both improve understanding of CAD and reduce the cost of treatment by providing more accurate physiological information through simulation. Recent efforts show potential to improve diagnosis of CAD [12] by using CFD methods for the estimation of FFR [13,14], which may avoid costly, uncomfortable and risky procedures of sedation, catheterization, and induction of hyperemia. CT angiography may identify stenoses and determine the geometry of the coronary vasculature. CFD simulations based on input data consisting of vascular geometry, and blood pressure and cardiac output may predict flow and pressure through the stenosed artery and thus also FFR (This approach is typically referred to as virtual FFR or vFFR).

Despite this tremendous potential, the necessity of appropriate boundary conditions (BC) and input data for CFD analysis remains an obstacle. Further, uncertainties about input data must be addressed to ensure the reliability and robustness of vFFR for clinical decision making.

CFD methods for vFFR typically solve standard equations of fluid mechanics over a domain generated from imaging data with BC based on direct measurements or physiologically motivated models which couple to CFD model. This approach requires input data consisting of geometric measurements, model parameters, and patient specific characteristics for imposition of BC. We investigated the effect of uncertainties about the input data for BC and geometric data for a simplified method of vFFR. This model integrates a detailed network of porcine coronary arteries (down to diameter of approximately 0.1 mm) [15] with a simple stenosis model [16]. To evaluate the influence of uncertainties, we employed polynomial chaos, metamodeling, and Monte Carlo methods in order to estimate the variability of vFFR estimates for assumed uncertainties about the model parameters, inputs and boundary conditions. We first developed a simplified model for coronary blood flow during hyperemia based on Murray's law and a stenosis model proposed by Huo et al. [16]. With this model we employed polynomial chaos quantify the effects of uncertainties in cardiac output, arterial pressure, and the internal model parameters. Subsequently, we used hierarchical modeling and Markov chain Monte Carlo to evaluate the discrepancy between observed geometrical diameters in our data set and the physiological diameters based on Murray's law. We evaluated the sensitivity of vFFR to such uncertain geometric measurements with metamodel based Monte Carlo sensitivity analysis. Finally, we evaluated the consequences of limited image resolution on the estimation of vFFR and developed a novel approach to infer the flow through vessels that do not appear in imaging data used for the prediction of vFFR.

2. Methods

To investigate the effects input data uncertainty on vFFR we developed a simplified model of coronary blood flow that is amenable to performing uncertainty quantification and sensitivity analysis, while preserving many of the characteristics of more complex models, i.e. dependence on geometric data and based on similar physical principles. We constructed a model of hyperemic flow in coronary arteries based on Murray's law (2), measurements of coronary artery geometry, cardiac output, arterial blood pressure, rheological parameters and myocardial flow fraction. The model consists of a system of nonlinear equations (9) that determines pressure in the coronary arteries and thus also, vFFR by (10).

We investigated the effects of uncertainty in clinical measurements and model parameters with polynomial chaos method. The impact of geometric uncertainties is assessed by first estimating the measurement error with a Bayesian Hierarchical modeling approach for the given data set and subsequently by employing a metamodeling approach combining random forest regression and polynomial chaos to estimate sensitivity indices for each arterial segment. Additionally, we assessed the impact of limited image resolution by comparing simulations using the full data set to simulations which include only vessels down to a certain threshold. Additionally, we proposed a new method to account for blood flow to vessels that do not appear in imaging data.

In the following we will first outline the model for estimating vFFR given geometric data and patient data and then detail each component of the model in more detail. Subsequently, we will present the methods of concepts used for UQ and SA. Finally, we will present the details for each analysis conducted.

2.1. Coronary blood flow model

We present a hemodynamical model based on the assumption of laminar and steady flow, and boundary conditions based on Murray's law [17]. Bulant et al. [18] recently compared predicted FFR for steady and unsteady 3D simulations and found less than 1% difference. Steady flow also allows the intramyocardial pressure, which varies over the cardiac cycle, to be neglected as its average effects are accounted for in the terminal resistances and assumed geometries.

Based on these assumptions we modeled coronary blood flow as a lumped parameter network of resistors with inflow, q, inlet arterial pressure, p_a, and venous pressure, p_v, at the outlets. In principle this model could be applied to any set of appropriate geometric measurements of coronary network anatomy, though we consider only a single network topology based on detailed geometrical data from a porcine heart [15]. The resistances are calculated using vessel dimensions and Poiseuille's law. To complete the model, a stenosis submodel based on the work of Huo et al. [16] is inserted into the coronary network, and the vFFR is calculated based on the complete network, boundary conditions, and flow distribution

models. The terminal resistances determined for the baseline network are scaled in order to reflect the usage of adenosine to induce hyperemia in patients when evaluating FFR. The following sections describe the geometric data and subsequently expand on each of components of these mathematical models of coronary blood flow.

2.1.1. Geometric data

Kassab et al. [15] made silicone elastomer casts of a porcine coronary network. From these casts they recorded detailed descriptions of the three main branches of the coronary network, i.e. the right coronary artery (RCA), the left coronary artery (LCA), and the circumflex artery (CX). The geometry of each branch is characterized by noting the length l and diameter d of the main trunk between each bifurcation. At each bifurcation the diameters of the outlets are also reported (see Fig. 1B), thus describing the main coronary branches as a sequence of vessel segments with outlets from the main trunk located at each junction. To explicitly represent this data, we define the set $\mathcal{N} = \{(d_i, l_i, \mathbf{b}_i)\}$ where i indexes the vessels from the inlet, $i = 0$, to the terminal segment, $i = n_s$, and $\mathbf{b}_i = (b_{i1}, \ldots, b_{in_i})$ is a list of the n_i outlet diameters at the junction of segments i and $i+1$. Superscript notation, $\mathcal{N}^{\Omega}$, denotes the set corresponding to a particular branch of the coronary arteries.

Porcine coronaries are widely used as a biological model of human coronaries and to a large extent the anatomies are similar, as well as the relative size in comparison total body size. Levolas et al. [19] review the similarities and differences of porcine and human hearts and conclude porcine hearts are the most appropriate biological model for cardiovascular research and that the hemodynamics are sufficiently similar for testing and evaluating methods and equipment intended for biomedical applications. The gross size of the heart and coronaries as well as the cardiac output are quite similar to those of humans, thus while not an exact match of hemodynamic patterns the general characteristics and driving factors are quite similar.

2.1.2. Hyperemic blood flow model

To predict FFR from a set of geometric measurements some sort of model, typically based on the underlying hemodynamics, must be employed to predict the pressures and flows in the coronaries. The model consists of a description of the hemodynamics within the domain where data is available and the determination of boundary conditions to describe the flows and or pressures at the inlets and outlets of the network.

First, the boundary conditions of the resting state are determined by assuming the flow to the coronaries is proportional to the cardiac output q_{co}

$$q_{\text{myo}} = \Lambda_{\text{myo}} q_{\text{co}}. \tag{1}$$

To determine the boundary conditions at the outlets, we applied Murray's law to determine the flow at each outlet. Murray's law [17] predicts that under resting conditions the flow in a given blood vessel is

$$q = a d^c, \tag{2}$$

where a is a coefficient determined by the relationship between viscous losses and metabolic demands and d is the vessel diameter. Applying this relationship to the outlet diameters and enforcing conservation of mass implies that

$$q_{\text{myo}} = \sum_{\Omega} \sum_{i} \sum_{j} a b_{ij}^c, \tag{3}$$

and thus the fraction of the q_{myo} that flows through the jth outlet at the junction of segments i and $i+1$ is

$$\frac{q_{ij}}{q_{\text{myo}}} = \frac{b_{ij}^c}{\sum_{\Omega} \sum_{i} \sum_{j} b_{ij}^c} \tag{4}$$

as the coefficient a cancels (b_{ij} is the diameter of the outlet). Similarly, the flow to a particular coronary branch is

$$q_{\Omega} = \sum_{i \in \mathcal{N}^{\Omega}} \sum_{j=1}^{n_i} \Lambda_{ij} q_{\text{myo}}, \tag{5}$$

where Ω is one of CX, LAD, or RCA, j denotes the segment index within $\mathcal{N}^{\Omega}$, and $\Lambda_{ij} = \frac{q_{ij}}{q_{\text{myo}}}$ is the flow fraction to a specific outlet.

Given the flow into a particular branch and the flow leaving at each junction, the flow in a particular segment is

$$q_{i+1} = q_i - \sum_{j} \Lambda_{ij} q_{\text{myo}}. \tag{6}$$

where q_{i+1} denote the flow from segment i to segment $i+1$.

These assumptions fully determine the flow through the coronaries. To determine the pressure distribution we assumed that the pressure at root of each coronary branch was simply the systemic arterial pressure p_a. Assuming each segment of coronary vasculature is cylindrical and blood flow is laminar and steady, the pressure drop along a particular segment of coronary vasculature is given by Poiseuille's law:

$$p_{i+1} - p_i = \frac{128 \mu l_i}{\pi d_i^4} q_i, \tag{7}$$

where μ is the viscosity of the blood, l_i is the length of the segment and d_i is the diameter of the segment. Eqs. (5)–(7) determine the flows and pressures in the coronary network in resting conditions.

The physiological principle behind FFR is to quantify the impact of stenosis as the amount that it impedes maximal physiological flow relative to a healthy vessel. Thus, hyperemic conditions are induced by pharmacologically dilating the coronary microvasculature and decreasing its resistance to flow to measure FFR. To simulate this, we assume the resistance to flow under hyperemia $R_{ij}^{hyp} = \alpha R_{ij}$ where R_{ij} is the outlet resistance in resting conditions and α is the total coronary resistance index (TCRI) corresponding to the amount the resistance is decreased during hyperemia. The resistance in resting conditions is calculated by applying Ohm's law $(p_{i+1} - p_v) = R_{ij} q_{ij}$, which implies

$$R_{ij} = \frac{p_{i+1} - p_v}{\Lambda_{ij} q_{\text{myo}}}, \tag{8}$$

where p_v is the venous pressure.

As adenosine primarily affects the myocardium, we assume as others have that R_{sys} does not change during induced hyperemia and further that q_{co} is constant [20,14]. The arterial pressure during hyperemia is $p_a = q_{\text{sys}} R_{\text{sys}}$, where $q_{\text{sys}} = q_{\text{co}} - q_{\text{myo}}$, and R_{sys} may be determined from the coronary flow, cardiac output and arterial pressure in resting conditions.

Instead of (7), the pressure loss across a stenosed segment is treated as a nonlinear function of flow, stenosis geometry, and rheological parameters of the blood, $p_{i+1} - p_i = f(q_i, d_i, d_s, l_s, \mu, \rho)$, as the simplifications due to assumed laminar and symmetric flow are violated in a stenosis, We employed a stenosis model developed and validated against occlusions of both human carotid and porcine coronary arteries ($R^2 = 0.9$ and $R^2 = 0.7$ respectively) by Huo et al. [16]. The function f is presented in detail in the appendix (Section A.1).

The reduced outlet resistances, the relationship between arterial pressure and systemic flow, and the stenosis model complete

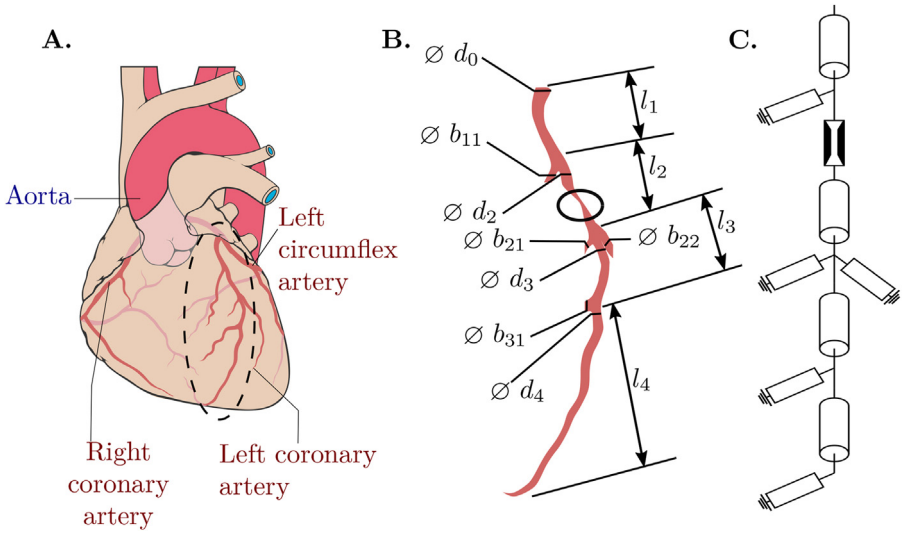

Fig. 1. Panel A shows the coronary arteries on the heart, panel B shows the extracted left coronary artery and associated dimensions, panel C shows the resulting lumped parameter model of resistances, a stenosis model, and terminal impedances. (Panels A and B modified from the work of Patrick J. Lynch, medical illustrator derivative work: Fred the Oyster adaption and further labeling: Mikael Häggström – with permission CC BY-SA 3.0.) Note the full coronary circulation imaged consists of three branches like the one shown in panel C.

the model of coronary flow during hyperemia, which imposes a pressure condition at the inlets of the coronaries and resistances at the outlets. The flows and pressures may be determined by satisfying these equations as well as the conservation of mass for each subnetwork $\mathcal{N}^{\text{CX}}$, $\mathcal{N}^{\text{LAD}}$, and $\mathcal{N}^{\text{RCA}}$. The system of equations is thus

$$
\begin{aligned}
q_{\text{myo}} &= q_{\text{CX}} + q_{\text{LAD}} + q_{\text{RCA}} \\
q_{\text{sys}} &= q_{\text{co}} - q_{\text{myo}} \\
p_a &= R_{\text{sys}} q_{\text{sys}} \\
q_{\text{myo}} &= \sum_{\Omega \in \text{CX,LAD,RCA}} \sum_{k \in \mathcal{N}^{\Omega}} \sum_{l=1}^{n_k} q_{kl} \\
q_{ij} &= \frac{p_{i+1} - p_v}{\alpha R_{ij}} \\
q_{i+1} &= q_i - \sum_{j}^{n_i} q_{ij} \\
p_{i+1} &= \begin{cases} p_i - f(q_i, d_i, d_s, l_s, \mu, \nu) & \text{if segment } i \text{ is stenosed} \\ p_i - \dfrac{128 \mu l_i}{\pi d_i^4} q_i & \text{otherwise.} \end{cases}
\end{aligned}
\tag{9}
$$

This nonlinear system of equations in terms of the flows to each branch of the coronary network and the nodal pressures may be solved using a nonlinear equation solver such as `fsolve` from the Python library `scipy.optimize`.

In summary given a nominal cardiac output q_{co}, arterial pressure p_a, and myocardial flow fraction Λ_{myo}, the outlet resistances may be determined from Eqs. (4)–(8). Additionally, the systemic resistance is determined by $R_{\text{sys}} = \frac{p_a}{(1-\Lambda_{\text{myo}})q_{\text{co}}}$. Once these have been calculated the stenosed model (9) is solved for the flows and pressures in each segment from which vFFR is calculated as

$$
\text{vFFR} = \frac{p_{i+1}}{p_a}, \tag{10}
$$

where segment i is the stenosed segment.

2.2. Generation of simulated CT-imaging based data

The geometry and topology used for vFFR depends on the vessels identified by segmentation of clinical imaging data. Thus, the limits of clinical CT-imaging resolution and vessel segmentation will prevent observation of vessels smaller than some threshold, d_{th}. Consequently, CT-imaging based vFFR will not account for any flow that goes through vessels smaller than this threshold. We simulated CT-angiography data by generating a new network $\mathcal{N}_{d_{th}}$ from the cast data consisting of only the outlets b_{ij} larger than a threshold d_{th}. To simulate the prediction vFFR from clinically derived imaging data, the same mathematical model, Eqs. (4)–(8) and (9) was applied using only the data in $\mathcal{N}_{d_{th}}$.

2.3. Method to estimate flow to unobserved vessels

As many vessels will not appear in imaging data, a method that compensates for this lack of information is highly desirable. We propose an extension to the model that estimates the amount of blood that "leaks" out of visible vessels through unobserved vessels in imaging data. The leaking blood flow may be accounted for by adding an outlet resistance to each observed vessel such that Murray's law, (3), is satisfied, i.e. $q_i = ad_i^c = \sum_j ab_{ij}^c + q_{i+1}$ where b_{ij} is the diameter of the jth outlet at the junction. The additional resistance is added by appending an additional outlet diameter $b_{i,\text{leak}}$ to $\mathbf{b}_i$ such that

$$
ad_i^c = \sum_j ab_{ij}^c + ab_{i,\text{leak}}^c + ad_{i+1}^c, \tag{11}
$$

which simplifies to

$$
b_{i,\text{leak}}^c = d_i^c - \sum_j b_{ij}^c - d_{i+1}^c. \tag{12}
$$

Once all $b_{i,\text{leak}}$ are determined, the same procedure as outlined in Section 2.1.2 may be applied to determine the network resistances, pressures and subsequently vFFR ($\text{vFFR}_{\text{leak}}$ is used to denote a vFFR calculated specifically using the leakage model). Note that the value $R_{i,\text{leak}} = \frac{p_{i+1}}{\Lambda_{i,\text{leak}} q_{\text{myo}}}$ represents the equivalent leakage resistance present at the junction between segments i and $i+1$.

2.4. Summary of models

We have presented a model of coronary blood flow based on physical principles, geometrical data and values for cardiac output, myocardial flow, and arterial pressure. The flow and pressure in the coronary network may be predicted for nominal and hyperemic conditions. These predictions also directly estimate vFFR. We have proposed method to simulate limited clinically derived geometric data, as well as a method that could be employed to infer the presence of vessels which do not appear in the explicit geometric data.

We will now present a number of methods for analysis of the effects of uncertainty in the input data. First we will introduce the basic concepts of uncertainty quantification and sensitivity analysis. Subsequently, we will describe the specific methods we employ in this study.

2.5. Uncertainty quantification and sensitivity analysis

We performed uncertainty quantification and sensitivity analysis (UQSA) of the coronary blood flow model using polynomial chaos, metamodeling and Monte Carlo algorithms. An overview of the primary concepts of UQSA may be found in the recent review by Eck et al. [21]. For cases with fewer than 10 input parameters we used polynomial chaos. When considering more input parameters, we employed Monte Carlo methods and further metamodeling in order to efficiently evaluate the sensitivity of the model. The characterization of input uncertainty is a key part of performing UQSA. Where possible we refer to known characterizations of measurement uncertainty, population variability, and reported ranges of model parameters to characterize the range of input parameters. In some cases inference of model parameters and associated uncertainties is performed based on the network data using hierarchical modeling. Detailed descriptions of the exact methods used and the statistical model for parameter estimation are reported in the subsequent sections.

As the specific methods are covered in detail in the referenced work, we present only the basic concepts and notation. The sources of uncertainty include measurement error, intrinsic biological variability, and assuming population or average values for unmeasured parameters. The model is treated as function of these inputs, $\mathbf{Z}$, which yields an output of interest Y. In this paper, the model output is Y = vFFR, while the model parameters and geometry data are the model inputs. A schematic diagram of the flow of data in uncertainty quantification and sensitivity analysis is given in Fig. 2. To conduct UQSA, first determine the probability distribution of $\mathbf{Z}$ to reflect the uncertainties, then calculate the distribution of Y by propagating $\mathbf{Z}$ through the model. The uncertainty of Y is characterized by its variance and associated tolerance intervals, $\left(Y_{\alpha/2}, Y_{1-\alpha/2}\right)$, containing to $(1-\alpha)\times 100$ percent of the probability density. Further the variance of Y is partitioned to calculate Sobol sensitivity indices S_i and S_{Ti} which quantify the amount of variance due to the ith component of $\mathbf{Z}$ [22,23]. S_i is the first order sensitivity index and quantifies the direct influence of Z_i while, S_{Ti} is the total sensitivity index which includes the average impact of Z_i including its interactions with other sources of uncertainty.

2.5.1. Polynomial chaos

Polynomial chaos expansions approximate a function of stochastic variables as a sum of multivariate basis polynomials orthogonal with respect to the joint probability distribution of the input variables [24]. Orthogonality enables more efficient calculation of uncertainty and sensitivity measures of the function in comparison to Monte Carlo methods for sufficiently low numbers of inputs. For an overview of UQSA methods and polynomial chaos expansions, we refer the reader to the recent paper on the UQSA for cardiovascular models [21]. We used the Python toolbox `chaospy` developed by Feinberg and Langtangen to perform polynomial chaos [25].

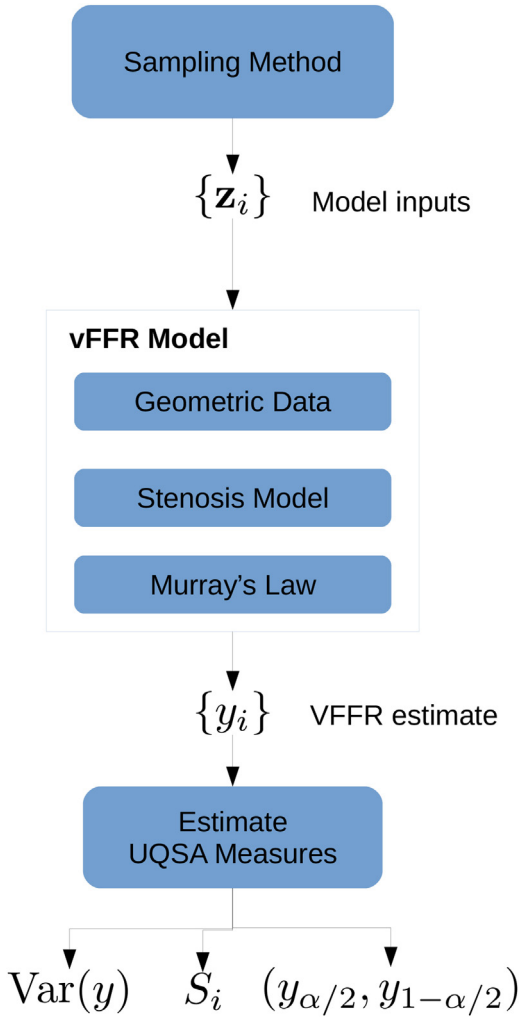

Fig. 2. Schematic of the flow of data and components in the modeling and uncertainty quantification framework.

2.5.2. Metamodel assisted Monte Carlo

For cases where a large number of model inputs vary independently it is no longer computationally efficient to use polynomial chaos as the number of terms – and thus model evaluations – grows rapidly with the number of inputs according to the binomial coefficient $\binom{D+p}{p} = \frac{(D+p)!}{p!D!}$ where D is the number of inputs and p is the polynomial order. Further, Monte Carlo methods may require a prohibitive amount of simulations before converging to accurate estimates of sensitivity indices. UQSA of models with large numbers of inputs thus requires alternative methods.

One approach is to approximate the model with a more efficient metamodel and to perform sensitivity analysis on this metamodel as a proxy for the full model. To estimate the uncertainty of vFFR due to uncertainties in individual diameters, we first created a metamodel of the full model using random forest regression [26] and subsequently estimated sensitivity indices of the outlet diameters by Monte Carlo methods applied to the metamodel [27,28]. A random forest metamodel provides a very efficient way to evaluate the large number of samples required for high dimensional Monte Carlo sensitivity analysis. With minimal tuning of the fitting procedure,

random forest regression also tends to achieve a good accuracy while avoiding overfitting [29]. Similar approaches for sensitivity analysis using metamodeling and Monte Carol estimation proved to agree qualitatively in terms of sensitivity indices [30,31].

A regression tree consists of a sequence of binary rules where the first branch is selected if $z > z_c$ and the second otherwise. For each stage select the variable z_i and cutoff z_c such that the values $\mu_> = \frac{1}{N_>}\sum_{z_i>z_c} f(\mathbf{z})$ and $\mu_< = \frac{1}{N_<}\sum_{z_i<z_c} f(\mathbf{z})$ minimize $\sum_{z_i>z_c} ||\mu_> - f(\mathbf{z})|| + \sum_{z_i<z_c} ||\mu_< - f(\mathbf{z})||$ where $||\cdot||$ can be an arbitrary error metric. $\mu_<$ and $\mu_>$ need not be simply the average either. The rules for each of the daughter branches are generated in the same way, but using only the data corresponding to each branch. This is continued down to a certain number of generations or until a certain error threshold is achieved for each leaf, i.e. a branch with no children, of the tree.

Random forest regression averages, N_f, regression trees created using different randomly selected subsets of the input parameters, e.g. only the values of z_1, z_3, and z_6 for one tree and z_1, z_4, z_5, and z_6 for another. Further, each tree is fit only to a random subsample of the data. The prediction is then the average of all of the individual predictions the N_f regression trees.

2.5.3. Parameter estimation and input uncertainty quantification

So far we have presented uncertainty quantification from the perspective of error propagation, yet the characterization of the uncertainty about the data and parameters is also important. In this study we employ Bayesian hierarchical modeling to estimate the uncertainty about the measured radii and Murray's exponent, c. In this approach, the data are assumed to follow a certain distribution conditioned on the values of the model input parameters, e.g. independent normally distributed values with mean value corresponding to the model

$$y_i \mid \boldsymbol{\theta}_i, \sigma_e \sim \mathcal{N}(m(\boldsymbol{\theta}_i), \sigma_e) \tag{13}$$

where y_i denotes the ith data point, m the model, $\boldsymbol{\theta}_i$ the model parameters' values for the ith data, and σ_e the error standard deviation. The relationship between parameters is described through a hierarchy of conditional distributions, e.g. $\boldsymbol{\phi} \mid \gamma \sim \mathcal{D}_\phi$, where $\mathcal{D}$ represents a hypothesized distribution of the parameter $\boldsymbol{\phi}$ conditional on γ. The number of levels can be chosen to accommodate the hypothesized relationships between the variables and parameters. For a more detailed description of Bayesian Hierarchical modeling, we refer the reader to Gelman et al. [32].

Given the hierarchy the distribution of the model parameters given the data is estimated based on Bayes' theorem

$$p(\boldsymbol{\theta}, \sigma_e \mid \mathbf{y}) = \frac{p(\boldsymbol{\theta}, \sigma_e, \mathbf{y})}{p(\mathbf{y})} = \frac{p(\mathbf{y} \mid \boldsymbol{\theta}, \sigma_e) p(\boldsymbol{\theta}, \sigma_e)}{p(\mathbf{y})}. \tag{14}$$

The hierarchical approach provides a conceptually simple way to build up $p(\mathbf{y} \mid \boldsymbol{\theta}, \sigma_e) p(\boldsymbol{\theta}, \sigma_e)$ as $p(\mathbf{y} \mid \boldsymbol{\theta}, \sigma_e)$ is determined by (13) and $p(\boldsymbol{\theta}, \sigma_e)$ by the $\mathcal{D}_\phi$. The posterior density of $\boldsymbol{\theta}$ and σ_e (the left hand side of (14)) quantifies the most characteristic values of the parameters based on the data as well as the uncertainty about these values, i.e. the width, variance or quantiles of this density. The denominator of the equation is defined by

$$\begin{aligned} p(\mathbf{y}) &= \int_{\Omega_\theta \times \Omega_e} p(\mathbf{y}, \theta, \sigma_e) d\theta d\sigma_e \\ &= \int_{\Omega_\theta \times \Omega_e} p(\mathbf{y} \mid \theta, \sigma_e) p(\theta, \sigma_e) d\theta d\sigma_e \end{aligned} \tag{15}$$

where Ω_θ and Ω_e denote the regions where $\boldsymbol{\theta}$ and σ_e have nonzero probability density. Direct evaluation of (14) requires calculation of this (potentially) high dimensional integral. Further, calculating the mean, median, standard deviation or percentiles of θ and σ requires evaluating similar integrals, e.g. $\mathrm{E}(\theta) = \int_{\Omega_\theta \times \Omega_e} \theta p(\theta, \sigma_e \mid \mathbf{y}) d\theta d\sigma_e$.

The direct evaluation of (15) may be avoided by sampling the posterior distribution and calculating the corresponding sample statistics. Markov chain Monte Carlo (MCMC) methods allow sampling the unknown posterior density by produce a chain of samples based on the likelihood function, $p(\mathbf{y} \mid \boldsymbol{\theta}, \sigma_e) p(\boldsymbol{\theta}, \sigma_e)$. The details of this process and a specific implementation are presented by Salvatier et al. [33] who developed the Python toolbox `PYMC3` for performing MCMC.

Table 1
Table of assumed input uncertainties for evaluation of the effects of parametric input uncertainty on vFFR. Uniform distributions are denoted by $\mathcal{U}$(min, max) and normal distributions $\mathcal{N}$(mean, std. dev.).

Input	Symbol	Nominal value	Distribution
Cardiac output	q_{co}	6 L/min	$\mathcal{N}(6, 1.0)$
Arterial pressure	p_a	93.0 mmHg	$\mathcal{N}(93, 4.77)$
Myocardial flow fraction	Λ_{myo}	0.045	$\mathcal{U}(0.04, 0.05)$
TCRI	α	0.23	$\mathcal{U}(0.15, 0.30)$
Murray's law exponent	c	3.0	$\mathcal{U}(2.4, 3.0)$
Hematocrit	H	0.45	$\mathcal{N}(0.45, 0.08)$

2.6. Analyses

We applied the aforementioned methods of uncertainty quantification and sensitivity analysis to the vFFR model for three specific analyses. First, we considered the impact of input data uncertainty in the absence of geometric uncertainty. Second, we employed MCMC to quantify the uncertainty about the geometric data and the parameter c in Murray's law, and then performed uncertainty quantification and sensitivity analysis of vFFR given geometric uncertainties based on the estimated parameters. Finally, we assessed the performance of the model for limited image resolution data and evaluated the performance of our newly proposed missing vessel correction method. Each analysis is presented in detail in the following sections.

2.6.1. Impact of non-geometric input uncertainties

To account for uncertainties about the model parameters and input values, we performed UQSA via the polynomial chaos approach. Using the whole coronary network model (see Section 2.1.2), we first considered the effects of parametric uncertainty on vFFR for a 75% area stenosis 1 mm long to replace segment 10 of the LAD, the entrance length was taken to be the length of the segment.

The values of the arterial pressure, cardiac output, myocardial flow split, TCRI, and hematocrit, which determines density and viscosity, were treated as uncertain inputs. We used Hammersley sampling to generate twice as many samples (924) as coefficients for a 5th order polynomial approximation in 6 input variables and estimated the coefficients using regression. Hammersley sampling was used due to its nested nature which is convenient for assessing convergence. The polynomial order was chosen such that we found the estimates of sensitivity indices were less than 1% different between successive orders. The primary quantities of interest were a 95% prediction interval for vFFR, and the sensitivity indices of vFFR for each input parameter. These were calculated from the polynomial chaos expansion.

We applied UQSA to understand the consequences of variability in input parameters and boundary conditions on the prediction of vFFR in clinical settings. To this end, we attempted to characterize the variation of these inputs according to clinical measurement modalities, and assumed a normal patient aside from the presence of the stenosis for characterizing the variability of unmeasured parameters. In the following section, we present the basis for the assumed input uncertainties summarized in Table 1 . Input dis-

tributions were characterized as either normal random variables when mean and standard deviation were given and as uniform random variables over the plausible range otherwise.

Arterial pressure. The sphygmomanometer is the current clinical standard for noninvasive blood pressure measurement. This method was found to have standard deviations of 3.3 mmHg and 5.5 mmHg in systolic and diastolic pressure measurement respectively [34]. The mean pressure is further approximated using the widely used formula $p_a = \frac{2}{3}p_d + \frac{1}{3}p_s$ [35], which, assuming perfect positive correlation between systolic and diastolic measurements has standard deviation 4.77 mmHg. We model the measurement of mean pressure as normal random variable with mean 93 mmHg and standard deviation 4.77 mmHg.

Cardiac output. The gold standard measurement of cardiac output requires invasive catheterization [36,37]; however, noninvasive methods derived from ultrasound show good agreement with invasive measurements [38]. Studies comparing ultrasound measurements to the pulmonary artery catheterization thermal dilution method have found the difference in measurements had a standard deviation of between 0.82 L/min and 1 L/min with mean biases were between 0.03 L/min and 0.18 L/min [39,40]. Based on these studies the clinical measurement of cardiac output was represented as normally distributed with a mean of 6 L/min a standard deviation of 1 L/min.

Myocardial flow fraction. Ideally the flow to the myocardium could be measured directly as recent studies have shown promise towards this end [41]; however, most of these methods require both dye injection and catheterization to accurately measure the volumetric flow. Thus, we assume the flow to the coronary arteries is a fraction of cardiac output, Λ_{myo}, which is between 4% to 5% on average [42].

Blood characteristics. The density ρ and viscosity μ of blood are important parameters in describing the mechanics of blood flow and both depend on hematocrit levels, H. Sankaran et al. [43] describe this using the relationship $\mu = \frac{\mu_p}{(1-H)^{2.5}}$ and note that a population average hematocrit of 0.45 with a standard deviation of 0.08. Blood density depends on hematocrit according to $\rho = \rho_e H + (1-H)\rho_p$, where the plasma density, ρ_p, is 1018 kg/m^{-3} and density of erythrocytes, ρ_e, is 1085 kg/m^{-3} [44]. We model ρ and μ according to these relationships and hematocrit as a normal random variable with the aforementioned mean and standard deviation.

2.6.2. Estimation of geometric uncertainty and its associated effect on vFFR

Given the available data it is of interest to estimate what values of the exponent c are plausible. Additionally, the small size of many arteries as well as the high pressure injection process used to producing a cast of the coronary arteries [15,45] could lead to discrepancies between the measured diameters and the physiological diameters. We employed Bayesian hierarchical modeling to formulate a statistical model that can account for uncertainty about both c and the true physiological diameters and estimate posterior probability distributions of c and the geometric uncertainty given the measured data using a Markov chain Monte Carlo method.

The measured diameters d_i were assumed to relate to the physiological diameters $\tilde{d}_i$ as

$$d_i = \tilde{d}_i(1 + E_i) \tag{16}$$

where E_i are independently and identically distributed normal random variables with mean 0 and standard deviation σ_e representing a proportional error of d_i relative to $\tilde{d}_i$. The likelihood of d_i given the physiological diameter $\tilde{d}_i$ and σ_e is simply a normal distribution with mean $\mu_i = \tilde{d}_i$ and standard deviation $\sigma_i = \sigma_e \cdot \mu_i$. Murray's law (3) implies that for physiological diameters $\tilde{d}_i = \left\{\sum_{j=i}^{n_s}\sum_{k=1}^{n_j}\left(\frac{b_{jk}}{1+E_{jk}}\right)^c\right\}^{\frac{1}{c}}$ where i indicates the inlet segment to a subnetwork $\mathcal{N}_i^{\Omega}$ consisting of the segments distal to and including segment i in branch Ω. Thus, the conditional distribution of d_i given the errors of the outlets, E_{jk}, and the Murray exponent, c, was specified for each subnetwork, $\mathcal{N}_i^{\Omega}$.

To complete the hierarchical model, we assumed uniform prior distributions for σ_e and c as little prior knowledge about the physiological diameters was available. The errors were assumed to be less than 50% for σ_e. For c the interval was (2, 4) corresponding to the range of values proposed in the literature. (We considered wider priors for c and σ_e, but it did not change the final inferences significantly.) Thus, the complete hierarchical model is

$$\begin{aligned}
\mu_i &= \left\{\sum_{j=i}^{k}\sum_{l=1}^{n_j}\left(\frac{b_{jl}}{1+E_{jl}}\right)^c + \tilde{d}_{k+1}^c\right\}^{\frac{1}{c}} \\
d_i \mid E_{ij}, c, \sigma_e &\sim \mathcal{N}(\mu_i, \sigma_e \cdot \mu_i) \\
E_{ij} &\sim \mathcal{N}(0, \sigma_e) \\
c &\sim \mathcal{U}(2, 4) \\
\sigma_e &\sim \mathcal{U}(0, 0.5)
\end{aligned} \tag{17}$$

To estimate the posterior distributions of σ_e and c given the measured diameters we performed a Markov chain Monte Carol simulation as described in Section 2.5.3 with the Python toolbox `PYMC3` [33]. The chain was run for one million steps and the posterior distributions for the average value of σ_e and c were characterized numerically from the Markov chain.

2.6.3. Impact of geometric input uncertainties

Due to the evidence of geometric uncertainty about the measured diameters inferred from the analysis of Murray's law presented in the previous section (Section 2.5.3), we considered the effect this uncertainty would have on vFFR. To assess the effects of these diametric uncertainties, we analyzed the same 75% area stenosis case as the previous analysis. A 1 mm long stenosis replaced segment 10 of the LAD. The pre-stenotic length was taken to be the length of the segment. The values of the outlet diameters were assumed to follow

$$\tilde{b}_{ij} = b_{ij}(1 + E_{ij}), \tag{18}$$

where E_{ij} are independently and identically distributed normal random variables with mean zero and standard deviation based on the mean of σ_e (0.073) from the Markov chain Monte Carlo analysis.

To construct the metamodel, we evaluated vFFR with the coronary model presented in Section 2.1.2 for 5000 different samples of the outlet diameters determined by Latin Hypercube sampling over the joint distribution of outlet diameters. (Latin hypercube sampling was chosen as it remains a Latin Hypercube sample as parameter dimensions are eliminated, i.e. well suited for each tree in the random forest.) We then fitted a random forest regression model to the values generated at these sample points with `RandomForestRegressor` from the Python package `scikit-learn` using the default parameters. The number of subtrees, 100, was selected to ensure sufficient accuracy of the meta-model such that the average out-of-bag error was less than 0.01 and the maximum absolute error was less than 0.02.

To estimate the sensitivity to particular outlet diameters, we computed the vFFR via the random forest to determine sensitivity indices of vFFR to each outlet based on the Monte Carlo algorithms proposed by Saltelli (for S_i) and Sobol (for S_T) with sample matrices **A** and **B** of 50,000 samples such that a difference of less than 10^{-3} was achieved between S_T for successive samples of 10,000 [46]. As

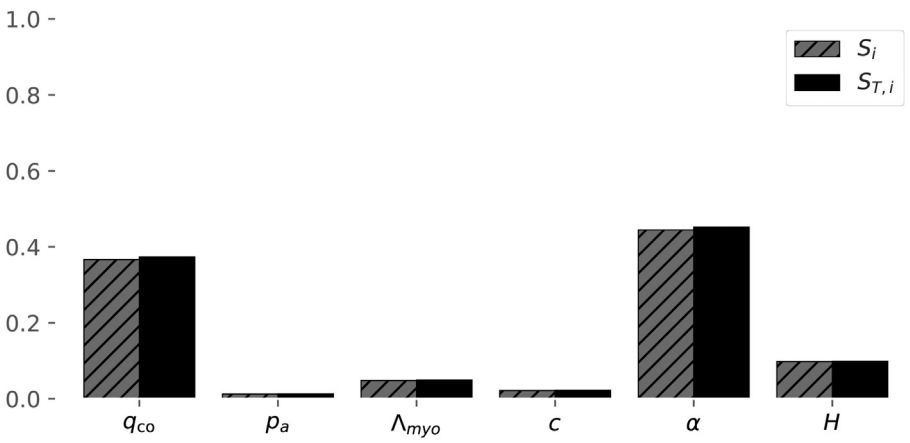

Fig. 3. Sobol sensitivity indices (first order gray with hatches and total black) for the full coronary artery model subjected to uncertainty across all input parameters. Cardiac output, Q, and TCRI, α, are the most significant inputs in the resulting uncertainty of vFFR.

a test of this approach, we compared polynomial chaos and the meta model approach on a small problem of only 6 inputs, such that PC was feasible, and found good agreement between the two approaches.

2.6.4. Analysis of the impacts of limited resolution imaging

Clinical assessment of coronary arteries is limited by the resolution of imaging modalities as well as the process of segmenting and identifying vessels from images. CT angiography can resolve objects around 0.5 mm in optimal conditions, but the resolution may be reduced to compensate for noise and in clinical settings is closer to 1 mm [47,48]. The process of segmentation requires good quality images over the length of the vessel and thus in most studies the vessels analyzed are typically larger that 1.5 mm [49–58].

To characterize the impact vessel resolution may have on vFFR, we employed the procedure outlined in Section 2.2 to simulate clinical imaging of the coronary network from which the cast data was obtained. As the impact of image resolution likely depends on the location of the stenosed segment, we evaluated vFFR from the imaging based network $\mathcal{N}_{d_{th}}$ for each possible location of a 75% area stenosis 1 mm long. The error due to the limited resolution was quantified by

$$\mathrm{RMSE}(d_{th}) = \sqrt{\frac{1}{N_s}\sum_{\Omega}\sum_{i}\mathrm{vFFR}(\mathcal{N}_{d_{th}}, \Omega, i) - \mathrm{vFFR}(\mathcal{N}, \Omega, i)} \qquad (19)$$

where $\mathrm{vFFR}(\mathcal{N}, \Omega, i)$ indicates the predicted value of vFFR given the network data $\mathcal{N}$ with a stenosis located in segment i of branch Ω and $N_s = 94$ is the total number of segments in all branches. As the threshold diameter for observed vessels is not an exact value, this error was calculated at various values of d_{th} from 0 mm to 2 mm to provide a more complete picture of the potential impact image resolution could have on predicted vFFR.

Just as the impacts of unobserved vessels were quantified by (19), the performance of the proposed leakage model, see Section 2.3, at a given visibility threshold was assessed in the same manner by comparing $\mathrm{vFFR}_{\mathrm{leak}}(\mathcal{N}_{d_{th}})$ and $\mathrm{vFFR}(\mathcal{N})$ for all possible stenosis locations of a 75% area stenosis 1 mm long.

2.7. Summary of methods

In summary we have presented a model of hyperemic flow in the coronary arteries based on Murray's law (2), measurements of coronary artery geometry, cardiac output, arterial blood pressure, rheological parameters and myocardial flow fraction. Our model consists of a system of nonlinear equations (9) which when solved for the nodal pressures may be used to calculate vFFR by (10). We then presented two methods for propagating uncertainty through this model. The polynomial chaos approach was applied to quantify uncertainty and sensitivity when assuming geometrical data was highly accurate. An approach using random forest regression to generate a metamodel was presented for quantification of uncertainty and sensitivity indices when assuming uncertainty about all outlet diameters. This approach is more suitable than polynomial chaos due to the large number of input parameters when considering 114 outlets. We also present a hierarchical model (17) to estimate the variability of the Murray coefficient c and the physiological diameters when assuming that Murray's law accurately represents the true physiology. We further presented a method for simulating the consequences of reduced image resolution by removing geometrical data below a certain threshold, as well as a method that corrects for missing geometrical data by estimating a leakage flow at each junction to account for flow through invisible vessels.

3. Results

We applied the methods presented in the previous section to perform three analyses of the consequences of uncertainties in data required for computing vFFR. First, we investigated the case where only the internal model parameters and inlet boundary conditions were treated as uncertain. Second, we simulated the consequences of low resolution imaging by comparing the vFFR model (Section 2.1.2) for full geometric data to the case where only geometric data corresponding to diameters larger than a threshold d_{th} which varied from 0 mm to 2 mm. Finally, we considered uncertainty about the geometry itself by evaluating the sensitivity of vFFR to errors in measurement of outlet diameters performed hierarchical modeling to estimate the discrepancy between measured diameters and physiological diameters based on Murray's law. The results of each of these investigations are presented in the following section.

3.1. Simple stenosis model

The uncertainty quantification of vFFR for a single stenosis in the LAD considered the cardiac output (q_{co}), aortic pressure (p_a), myocardial flow fraction (Λ_{myo}), Murray's law exponent (c), hyperemic resistance coefficient (α), and hematocrit (H) as sources of uncertainty. These were based on the range of values reported in the literature reviewed in the methods section and summarized in Table 1 . The resulting estimate of vFFR had mean 0.78 and 95% prediction interval of (0.59, 0.90), note the threshold for clinical significance of 0.75. Fig. 3 shows first order and total Sobol sensi-

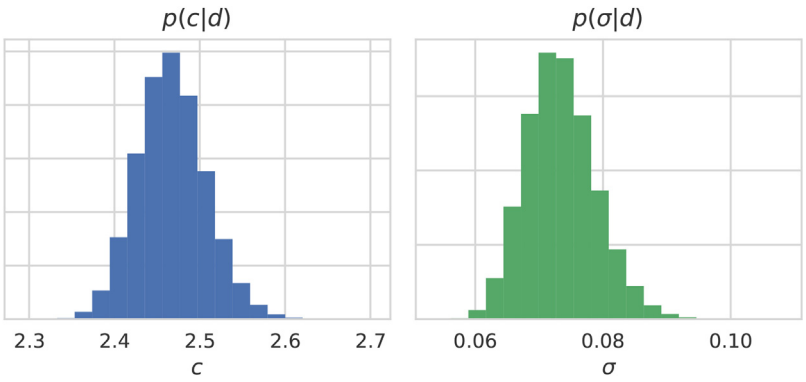

Fig. 4. Posterior distributions of Murray's law coefficient c and standard deviation σ of the error between measured and physiological diameters estimated using Markov Chain Monte Carlo (see 2.5.3).

tivity indices calculated from the polynomial expansion of which the measurements of cardiac output (q_{co}) and the estimate of TCRI (α) were the largest sources of uncertainty. Interesting is the fact that arterial pressure and the Murray's law coefficient c contribute almost no uncertainty, suggesting that the exact value of the Murray's law coefficient is not so important in determining vFFR.

3.2. Estimation of variability based on Murray's law

Since Murray's law provides the basis of determining outflows for the simulation of blood flow through the coronary vasculature, it is of interest to evaluate the accuracy of this principle with respect to the geometric data, and in particular to estimate the best fit of the exponent c, as well as to quantify the uncertainty about this estimate. We employed Markov Chain Monte Carlo to perform Bayesian parameter estimation for the hierarchical model of Murray's law and diameter uncertainty (see (17) and Section 2.5.3). Fig. 4 shows the resulting posterior distributions where c has mean 2.47 and standard deviation 0.040, and σ_e has mean 0.073 and standard deviation 0.005. These results suggest that differences between physiological diameters and measured diameters are somewhat uncertain, whereas the exponent value of c is fairly certain (standard deviation of less than 2% of the mean value) given this data.

3.3. Uncertainty quantification and Sensitivity Analysis given uncertain radii

To evaluate the impact of geometric measurement errors, we performed metamodel based sensitivity analysis for an LAD stenosis subject to uncertain measurements of outlet diameters. The sensitivity of vFFR to each outlet is shown in Fig. 5, where all sensitivities have been grouped into five bins according to sensitivity from very low sensitivity (the lowest 20%) to very high (the highest 20%). The absolute sensitivities are also shown in Fig. 6 with respect to the diameter of the outlet and position relative to the stenosis in the LAD. The larger the artery the more influential it is on the prediction of vFFR, while it also seems the relationship between diameter and sensitivity is steeper for vessels in the same coronary branch as the stenosis. Finally, the vessels distal to the stenosis were on average also markedly more influential on vFFR than those proximal.

3.4. Effect of unobserved vessels due to limited resolution

The impact of imaging limitations of clinical imaging was assessed by simulating reduced resolution data as described in Sections 2.2 and 2.6.4. For a visibility threshold of $d_{th} = 1.5$ mm and

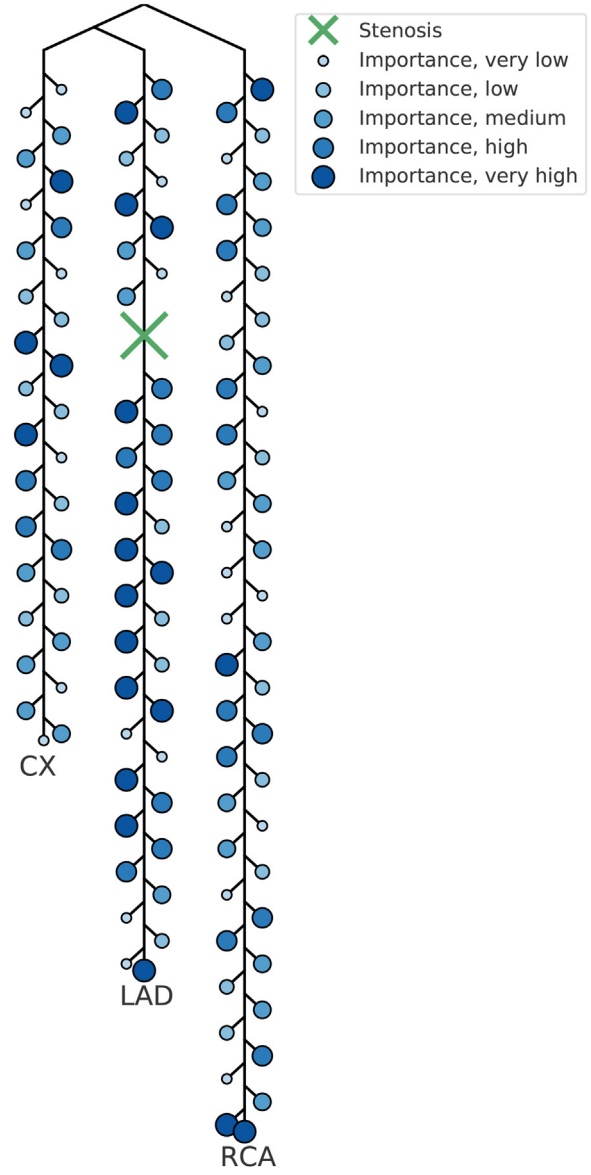

Fig. 5. Coronary tree with a stenosis in the upper LAD and outlets grouped after the relative importance according to the total Sobol indices calculated using a metamodel and Monte Carlo estimation. Each circle indicates an outlet of the network, and the larger and darker the circle indicate vFFR is more sensitive to uncertainty in the diameter of that particular outlet. The smallest circles indicate the sensitivity to those outlets was among the bottom 20% of all outlets, the largest circles indicates those outlets ranked in the top 20% of outlets. The sizes in between thus correspond to vessels falling between the 20th and 40th, the 40th and 60th, and the 60th and 80th percentiles respectively.

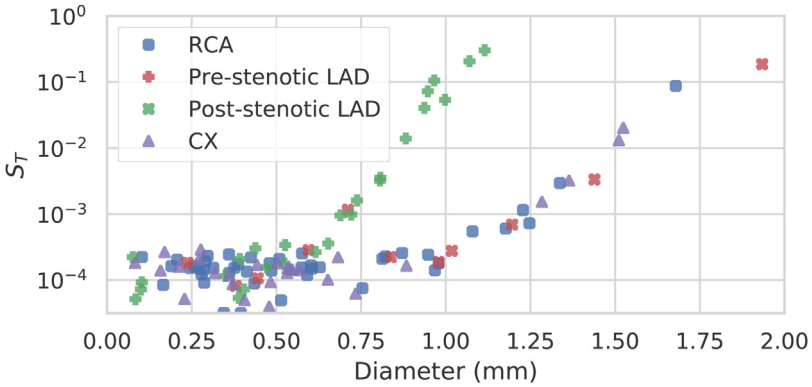

Fig. 6. Total Sobol sensitivity indices of vFFR to uncertainty in the radii of outlets in the coronary tree with a stenosis in the upper LAD. Sensitivity indices are plotted according to reported vessel diameter from [15].

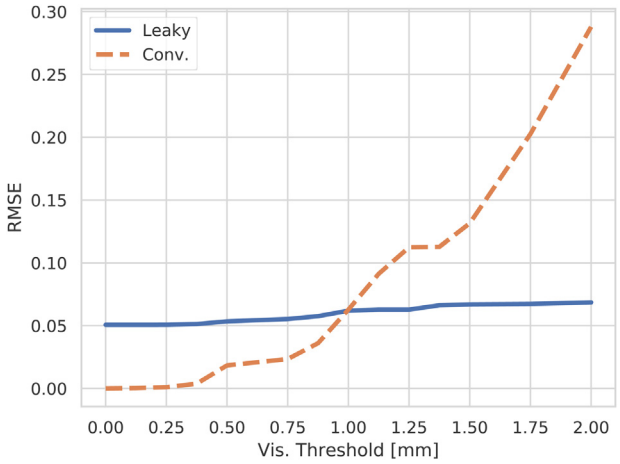

Fig. 7. The RMSE of vFFR relative to full visibility is shown for the conventional approach (dashed orange) and for the corrective model (solid blue) at different values of the visibility threshold, d_{th}.

stenoses of 75% area, the RMSE (19) was 0.131. The RMSE was further characterized over a range of d_{th} as shown in Fig. 7.

The leakage model to account for unobserved outlets (see Section 2.3) was assessed on the same cases simulating clinical imaging data. The RMSE of $\text{vFFR}_{\text{leak}}$ calculated with this correction for $d_{th} = 1.5$ mm was 0.067. The RMSE was also calculated over a range of values of d_{th} as shown in Fig. 7.

In this analysis the vFFR values predicted by $\text{vFFR}(\mathcal{N}_{d_{th}})$ and $\text{vFFR}_{\text{leak}}(\mathcal{N}_{d_{th}})$ were compared to the reference case $\text{vFFR}(\mathcal{N})$. The 1.5 mm threshold is motivated by clinical limitations, but it is not a precise cutoff below which no vessels are observed. Consequently, the dependence of the error in vFFR on the exact value of the threshold is of interest. To address this, the same analysis was applied at numerous values of d_{th} from 0 mm to 2 mm, corresponding to full visibility and no outlets visible, respectively. The resulting RMSE of $\text{vFFR}(\mathcal{N}_{d_{th}})$ and $\text{vFFR}_{\text{leak}}(\mathcal{N}_{d_{th}})$ are shown in Fig. 7. Further the difference between the conventional approach and the corrective, leaky vessel approach was characterized on a per vessel basis by comparing the error of the two approaches for stenoses located in each particular vessel (see Fig. 8).

4. Discussion

This study considered three categories of uncertainties relevant to simulations of coronary blood flow: parametric uncertainty in boundary conditions, geometric uncertainty of blood vessels in the domain, and topological uncertainty due to limited imaging resolution. The focus of this analysis was to quantify how uncertainties about the inflows and outflows of the whole network as well as the uncertainties about underlying hemodynamical parameters may affect the prediction of vFFR in general. As such, we performed sensitivity analysis on a simplified model of coronary blood flow that allowed a large number of simulations to be performed, while also retaining dependence on similar input data and assumptions as more sophisticated models. Some other studies of uncertainty quantification of vFFR have been performed by Sankaran et al. [43] and Eck et al. [21]. These studies have consistently found the cross-section of the stenosis as the most important parameter as opposed to rheological parameters or stenosis length. Sankaran et al [43] also considered uncertainty about the outlet resistance and found it to have similar though slightly smaller influence on vFFR in comparison to the cross-section of the stenosis; however, they did not account for uncertainties in the inflow boundary condition. As previous studies primarily focused on the characterization of the stenosis itself, and less on the determination of boundary conditions for prediction of vFFR, our results contribute a missing piece of analysis to the field.

The uncertainties of boundary model parameters were based on state of the art clinical measurement modalities where applicable, and literature survey of population and study-to-study variability otherwise. Subject to these uncertainties the model's predictions of vFFR had significant uncertainties and were unable to confidently determine if the 75% area reduction is clinically significant according to the cutoff value of 0.75 identified by the study of Tonino et al. [7] as the model's 95% prediction interval spanned from 0.59 to 0.90. Sensitivity analysis of this case indicated that the measurement of cardiac output, which determines myocardial inflow, and the degree of hyperemia induced influenced vFFR to the greatest extent of the all parameters considered in our analysis of boundary condition parameter uncertainty (see Fig. 3). Since the sensitivity of vFFR to the myocardial flow was quite large, it would be advantageous to improve determination of the total inflow to the myocardium, and if possible to better characterize the determinants of adenosine's efficacy at inducing hyperemia. Perhaps improved imaging modalities such as PET-MRI will become clinically feasible in the future [59], allowing direct measurement of coronary blood flow; however, they are currently not widely used due to the increased radiation exposure and expense. Basic investigation of myocardial response to adenosine could elucidate procedures to better characterize individual patient's coronary vasodilation.

The value of vFFR predicted was much less sensitive to underlying rheological parameters or the exponent c from Murray's law, even though this exponent is quite varied in the literature. Since the sensitivity of vFFR to these parameters is quite low,

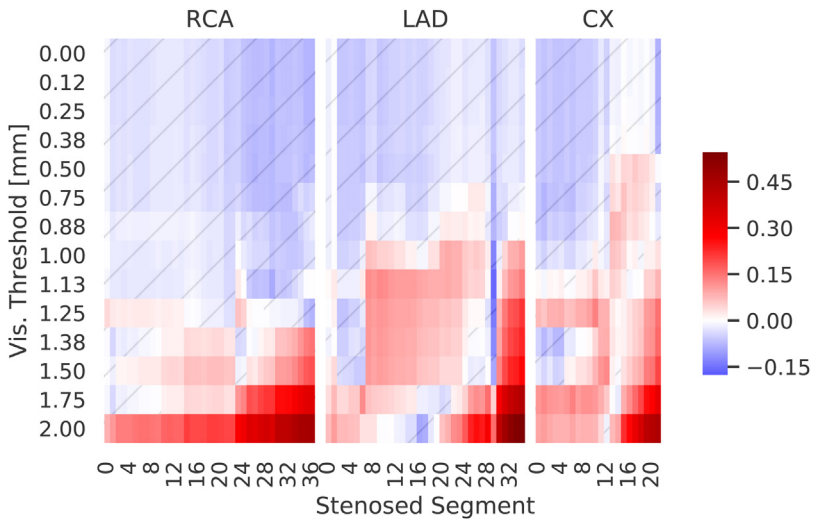

Fig. 8. Difference in the error of the conventional and corrected vFFR estimate, $\left|\text{vFFR}(\mathcal{N}_{d_{th}}, \Omega, i) - \text{vFFR}(\mathcal{N}, \Omega, i)\right| - \left|\text{vFFR}_{\text{leak}}(\mathcal{N}_{d_{th}}, \Omega, i) - \text{vFFR}(\mathcal{N}, \Omega, i)\right|$, shown on per vessel basis vs visibility threshold. Red indicates the conventional estimate of vFFR is worse than $\text{vFFR}_{\text{leak}}$ based on correction for invisible vessels. Blue hatched regions indicate the conventional vFFR was more accurate than vFFRleak.

efforts for improving the confidence of vFFR should not focus on characterizing these physical model parameters more accurately, rather the focus should be on providing accurate inflow conditions and determining the peripheral vasculature's response to induced hyperemia.

Our analysis of the fit of Murray's law to the geometric data for the porcine artery suggested that the mismatch between Murray's law and the reported geometry may be explained by errors in measurement of the diameters of vessels, while the uncertainty about the estimated exponent c is quite low relative to the range of values found in the literature. The mean value of 2.47 lies within, but on the lower end of, the range reported by various previous analyses [17,60–63].

However, as our analysis shows c only influences vFFR marginally (see Fig. 3), the more interesting results is that Murray's law suggests discrepancy between the observed values of vessel diameters and the values in physiological conditions. The discrepancy may be due to deviations from physiological conditions induced by the creation of the elastomer cast as noted by Suwa et al. [45], or simply due to measurement errors. In any case the findings above emphasize the importance of accurate measurement of the cross-sectional diameter of the vasculature as this can greatly influence the flow predicted through a given vessel.

Given the likely uncertainty in outlet diameters evaluation of our sensitivity analysis of vFFR to such measurements is particularly relevant. This analysis of vFFR with respect to outlet diameters shows two trends. First uncertainty in larger vessels is more influential relative to smaller vessels (see Fig. 6). Second the influence of vessels distal to the stenosis are markedly more influential than vessels of similar diameter proximal to the stenosis or in other branches of the network. These results emphasize the importance of identifying and segmenting larger vessels accurately, and that measurement and characterization of the vasculature distal to the stenosis seems to be of far greater importance than characterizing the proximal vasculature or the vasculature in other branches of the coronary network.

Analysis of geometric uncertainty naturally leads to consideration of different layers of uncertainty in geometric data, i.e. physical limitations of imaging, segmentation processing, and smoothing of computational domains. Identifying how much uncertainty each layer contributes would be a valuable contribution, albeit difficult. This is particularly true regarding image segmentation and generation of computational domains, as there are not generally absolute measurements available for estimation of the error. To our knowledge no studies have been conducted that systematically determine the contributions of each of these stages of image processing for computational simulations. Some studies have used interobserver variability as a metric for comparing performance of automated algorithms [64], and Bulant et al. [18] compared the vFFR resulting from CT and IVUS data in the same patients. They found the results were quite similar for both imaging modalities suggesting that uncertainties due to physical limitations of imaging modalities are not drastically affecting the resulting simulations.

Since the resolution of clinical imaging of coronary vasculature is limited, clinically reliable methods of estimating vFFR must account for the effect of this threshold to ensure the estimates are robust to variations in image quality. Imaging modalities and subsequent processing, such as segmentation, are encumbered by limitations of the level of detail that may be resolved. Thus, many vessels below a certain diameter will not be represented in the simulations. To evaluate the effect of this limitation, we compared the results of our estimation of vFFR using the high resolution data from the elastomer cast to the predicted vFFR based on lower resolution data consisting of only vessels of diameter larger than a threshold d_{th} between 0 mm and 2 mm (see Fig. 7). The results demonstrate that lack of detailed diameter observations results in an RMSE that substantially increases for $d_{th} > 1\ mm$ and attains a value of 0.131 if $d_{th} = 1.5$ mm, a clinically relevant cutoff value. These results suggest that the impacts of unobserved outlets may be substantial for models that distribute flow according to observed outlets and efforts should be made to mitigate the impact.

We proposed one such method (see Section 2.3) which applies the principle of Murray's Law (3) to account for invisible vessels. Our method estimates an expected leakage flow based on the disagreement between the imaged vessels and Murray's law (12). We applied our method to the same cases considered for evaluating the effects of limited resolution. The RMSE of the proposed method is shown in Fig. 7 at various values of d_{th} between 0 mm and 2 mm. The corrective method performs markedly better if d_{th} is somewhat larger than 1 mm. For $d_{th} = 1.5$ mm the RMSE was 0.067 or 48% lower than for the uncorrected approach. Comparing the conventional and corrective approach on a per vessel basis shows an increased benefit of the leaky vessel approach for stenoses located in the distal regions of the coronary vasculature (see Fig. 8). This pattern could

allow some stratification of when the corrective approach should be used as opposed to relying on uncorrected data.

While modern clinical CT can theoretically resolve objects as small as 0.5 mm in practice clinical imaging will only resolve vessels larger than 1 mm, and in some situations a coarser resolution is recommended to reduce image noise [48]. Further, segmentation of blood vessels requires a more consistent image than mere observation, so in practice most CT based assessment of coronary arteries considers only vessels with reference diameters larger than about 1.5 mm [49–58]. Therefore, in the context of noninvasive CT based vFFR, many vessels below 1.5 mm will not be segmented, and 1.5 mm can be treated as a clinical threshold for comparing the performance of vFFR methods.

Notably, the leaky vessel method is more stable over the range of visibility thresholds (see Fig. 7), whereas the conventional approach becomes worse as visibility degrades. This stability could be preferable even if the conventional approach is at times more accurate. Further, the leaky vessel model can be considered to not only account for missing vessels but also to correct for inaccurately dimensioned vessels and thus provide stability in the presence of uncertainties in clinical imaging and segmentation.

Further, as the essence of our method is the application of a simple physical principle to infer missing data, it is reasonable to investigate if such an approach may be applicable to a wide number of problems where underlying physical principles may be known, but measurement methods limit the resolution of certain details required for accurate modeling and simulation. This method is quite simple compared to some similar methods such as suggested by He and Xiu for model correction based on physical constraints [65], thus further development might result in more accurate and reliable means to account for missing information.

4.1. Conclusion

We analyzed the impacts of boundary condition, geometric and topological uncertainties on computational estimation of vFFR to quantify the uncertainty present given current clinical measurement modalities, and to further identify areas for focused effort to reduce that uncertainty. The results suggest two critical sources of variability in boundary conditions are the assumed flow into the coronary network, and the estimated reduction in resistance due to adenosine induced hyperemia. One focus to enable vFFR in the clinic would emphasize accurate determination of coronary blood flow. Another is to improve methods to predict patient specific hyperemic response, which could significantly reduce uncertainty in vFFR.

Sensitivity of vFFR to uncertainties in outlet diameters showed two patterns relevant to the management of geometric uncertainty for vFFR. First, the larger vessels are more influential, and second, vessels distal to the stenosis are much more influential than those proximal or in other branches than the stenosis. Thus, it may be more important to accurately assess the large vessels and local geometry around the stenosis than it is to improve the geometric measurements of the whole network. This focus could alleviate costs associated with processing or reprocessing the data, as well as potentially reducing the necessary computation domain.

Finally, we considered the impact of limitations on clinical imaging of coronary arteries and found vFFR estimates for limited resolution data deviated substantially from vFFR estimates using the full cast data. This suggests that the vessels missing from clinical images may be of some importance to accurately and consistently predicting FFR. To this end we encourage further development of methods to compensate for limited image resolution. One such approach, exemplified by our proposed method, is to use physically based physiological models to infer missing information. The results we found suggest this may be a promising approach for simulation of patient specific physiology from limited patient data, which in turn could enable improved clinical practice based on physiological simulation.

Appendix A

A.1 Huo et al. model of a stenosis

The model of Huo et al. [16] predicts a pressure drop Δp:

$$\Delta p = \frac{\rho q^2}{2}\left(\Delta p_c + \Delta p_d + \Delta p_e\right) + \Delta p_v, \tag{20}$$

where Δp_c, Δp_d, Δp_e and Δp_v represent the convective, diffusive, expansion and viscous pressures losses.

The convective contribution is given by:

$$\Delta p_c = \frac{1}{A_d^2} - \frac{1}{A_p^2}. \tag{21}$$

The diffusive and expansion pressures losses depend on the length of the stenosis (l_s). A dimensionless radius r' is introduced for the entrance region of the stenosis:

$$l_s = \frac{\rho q}{\pi\mu}\int_{r'}^{1} \frac{(1-r)(6+r)(1+4r+9r^2+4r^3)}{5r(3+2r)(3+2r+r^2)^2}dr \tag{22}$$

For $r' \geq 0.05$, the diffusive pressure drop is given by:

$$\Delta p_d^{r'\geq 0.05} = \frac{1}{A_s^2}\frac{96}{5}\int_{r'}^{1} \frac{1+4r+9r^2+4r^3}{r(3+2r)(3+2r+r^2)^2}dr \tag{23}$$

where $l_v = l_p + l_s + l_d$, and l_p and l_d are the lengths of vessel proximal and distal to the stenosis and l_s is the stenosed length. The expansion pressure drop is given by:

$$\begin{aligned}\Delta p_e^{r'\geq 0.05} &= \left(\frac{1}{A_s} - \frac{1}{A_d}\right)^2 + (1-r')^2 \\ &\times \left[2\left(\frac{1}{A_s} - \frac{1}{A_d}\right)\left(\frac{1}{A_s} - \frac{1}{3A_d}\right) - \left(\frac{1}{A_s} - \frac{1}{A_d}\right)^2\right].\end{aligned} \tag{24}$$

On the other hand, if $r' < 0.05$, the entrance length is first calculated as:

$$l_e = \frac{\rho q}{\pi\mu}\int_{0.05}^{1} \frac{(1-r')(6+r')(1+4r'+9r'^2+4r'^3)}{5r'(3+2r')(3+2r'+r'^2)^2}dr' \tag{25}$$

Then, the diffusive pressure drop is given by:

$$\Delta p_d^{r'<0.05} = \frac{1}{A_s^2}\frac{96}{5}\int_{0.05}^{1} \frac{1+4r'+9r'^2+4r'^3}{r'(3+2r')(3+2r'+r'^2)^2}dr'. \tag{26}$$

The expansion pressure drop is given by:

$$\Delta p_e^{r'<0.05} = 2\left(\frac{1}{A_s} - \frac{1}{A_d}\right)\left(\frac{1}{A_s} - \frac{1}{3A_d}\right). \tag{27}$$

The viscous pressure loss is given by

$$\Delta p_v = \begin{cases} \displaystyle\int_0^{l_v-l_e} \frac{8\pi\mu}{A^2}q\,dx & \text{if } r' < 0.05 \\ \displaystyle\int_0^{l_v-l_s} \frac{8\pi\mu}{A^2}q\,dx & \text{if } r' \geq 0.05 \end{cases} \tag{28}$$

References

[1] N.D. Wong, Epidemiological studies of CHD and the evolution of preventive cardiology, Nat. Rev. Cardiol. 11 (5) (2014) 276–289, http://dx.doi.org/10.1038/nrcardio.2014.26.
[2] WHO | Cardiovascular Diseases (CVDs). http://www.who.int/mediacentre/factsheets/fs317/en/.

[3] P.A. Heidenreich, J.G. Trogdon, O.A. Khavjou, J. Butler, K. Dracup, M.D. Ezekowitz, E.A. Finkelstein, Y. Hong, S.C. Johnston, A. Khera, D.M. Lloyd-Jones, S.A. Nelson, G. Nichol, D. Orenstein, P.W.F. Wilson, Y.J. Woo, Forecasting the future of cardiovascular disease in the United States, Circulation 123 (8) (2011) 933–944, http://dx.doi.org/10.1161/CIR.0b013e31820a55f5.

[4] D. Mozaffarian, E.J. Benjamin, A.S. Go, D.K. Arnett, M.J. Blaha, M. Cushman, S. de Ferranti, J.-P. Després, H.J. Fullerton, V.J. Howard, M.D. Huffman, S.E. Judd, B.M. Kissela, D.T. Lackland, J.H. Lichtman, L.D. Lisabeth, S. Liu, R.H. Mackey, D.B. Matchar, D.K. McGuire, E.R. Mohler, C.S. Moy, P. Muntner, M.E. Mussolino, K. Nasir, R.W. Neumar, G. Nichol, L. Palaniappan, D.K. Pandey, M.J. Reeves, C.J. Rodriguez, P.D. Sorlie, J. Stein, A. Towfighi, T.N. Turan, S.S. Virani, J.Z. Willey, D. Woo, R.W. Yeh, M.B. Turner, Heart disease and stroke statistics—2015 update: a report from the American Heart Association, Circulation 131 (4) (2015) e29–e322, http://dx.doi.org/10.1161/CIR.0000000000000152.

[5] N.H.J. Pijls, B.V. Gelder, P.V. der Voort, K. Peels, F.A.L.E. Bracke, H.J.R.M. Bonnier, M.I.H.E. Gamal, Fractional flow reserve, Circulation 92 (11) (1995) 3183–3193, http://dx.doi.org/10.1161/01.CIR.92.11.3183.

[6] B. de Bruyne, J. Bartunek, S.U. Sys, N.H.J. Pijls, G.R. Heyndrickx, W. Wijns, Simultaneous coronary pressure and flow velocity measurements in humans, Circulation 94 (8) (1996) 1842–1849, http://dx.doi.org/10.1161/01.CIR.94.8.1842.

[7] P.A. Tonino, B. De Bruyne, N.H. Pijls, U. Siebert, F. Ikeno, M. van 't Veer, V. Klauss, G. Manoharan, T. Engstrøm, K.G. Oldroyd, P.N. Ver Lee, P.A. MacCarthy, W.F. Fearon, Fractional flow reserve versus angiography for guiding percutaneous coronary intervention, N. Engl. J. Med. 360 (3) (2009) 213–224, http://dx.doi.org/10.1056/NEJMoa0807611.

[8] G.J.W. Bech, B.D. Bruyne, N.H.J. Pijls, E.D. de Muinck, J.C.A. Hoorntje, J. Escaned, P.R. Stella, E. Boersma, J. Bartunek, J.J. Koolen, W. Wijns, Fractional flow reserve to determine the appropriateness of angioplasty in moderate coronary stenosis, Circulation 103 (24) (2001) 2928–2934, http://dx.doi.org/10.1161/01.CIR.103.24.2928.

[9] B. De Bruyne, N.H. Pijls, B. Kalesan, E. Barbato, P.A. Tonino, Z. Piroth, N. Jagic, S. Möbius-Winkler, G. Rioufol, N. Witt, P. Kala, P. MacCarthy, T. Engström, K.G. Oldroyd, K. Mavromatis, G. Manoharan, P. Verlee, O. Frobert, N. Curzen, J.B. Johnson, P. Jüni, W.F. Fearon, Fractional flow reserve-guided PCI versus medical therapy in stable coronary disease, N. Engl. J. Med. 367 (11) (2012) 991–1001, http://dx.doi.org/10.1056/NEJMoa1205361.

[10] B. Hannawi, W.W. Lam, S. Wang, G.A. Younis, Current use of fractional flow reserve: a nationwide survey, Tex. Heart Inst. J. 41 (6) (2014) 579–584, http://dx.doi.org/10.14503/THIJ-13-3917.

[11] P.D. Morris, D. Ryan, A.C. Morton, R. Lycett, P.V. Lawford, D.R. Hose, J.P. Gunn, Virtual fractional flow reserve from coronary angiography: modeling the significance of coronary lesions: results from the VIRTU-1 (VIRTUal Fractional Flow Reserve From Coronary Angiography) study, JACC: Cardiovasc. Interv. 6 (2) (2013) 149–157, http://dx.doi.org/10.1016/j.jcin.2012.08.024.

[12] T. Kimura, H. Shiomi, S. Kuribayashi, T. Isshiki, S. Kanazawa, H. Ito, S. Ikeda, B. Forrest, C.K. Zarins, M.A. Hlatky, B.L. Norgaard, Cost analysis of non-invasive fractional flow reserve derived from coronary computed tomographic angiography in Japan, Cardiovasc. Interv. Ther. 30 (1) (2015) 38–44, http://dx.doi.org/10.1007/s12928-014-0285-1.

[13] C.K. Zarins, C.A. Taylor, J.K. Min, Computed fractional flow reserve (FFTCT) derived from coronary CT angiography, J. Cardiovasc Transl. Res. 6 (5) (2013) 708–714, http://dx.doi.org/10.1007/s12265-013-9498-4.

[14] C.A. Taylor, T.A. Fonte, J.K. Min, Computational fluid dynamics applied to cardiac computed tomography for noninvasive quantification of fractional flow reserve: scientific basis, J. Am. Coll. Cardiol. 61 (22) (2013) 2233–2241, http://dx.doi.org/10.1016/j.jacc.2012.11.083.

[15] G.S. Kassab, C.A. Rider, N.J. Tang, Y.C. Fung, Morphometry of pig coronary arterial trees, Am. J. Physiol. – Heart Circ. Physiol. 265 (1) (1993) H350–H365.

[16] Y. Huo, M. Svendsen, J.S. Choy, Z.-D. Zhang, G.S. Kassab, A validated predictive model of coronary fractional flow reserve, J. Roy. Soc. Interface 9 (71) (2012) 1325–1338, http://dx.doi.org/10.1098/rsif.2011.0605.

[17] C.D. Murray, The physiological principle of minimum work, Proc. Natl. Acad. Sci. U. S. A. 12 (3) (1926) 207–214.

[18] C. Bulant, P. Blanco, G. Maso Talou, C.G. Bezerra, P. Lemos, R. Feijóo, A head-to-head comparison between CT- and IVUS-derived coronary blood flow models, J. Biomech. 51 (2017) 65–76, http://dx.doi.org/10.1016/j.jbiomech.2016.11.070.

[19] P.P. Lelovas, N.G. Kostomitsopoulos, T.T. Xanthos, A comparative anatomic and physiologic overview of the porcine heart, J. Am. Assoc. Lab. Anim. Sci.: JAALAS 53 (5) (2014) 432–438.

[20] P. Sharma, L. Itu, X. Zheng, A. Kamen, D. Bernhardt, C. Suciu, D. Comaniciu, A framework for personalization of coronary flow computations during rest and hyperemia, 2012 Annual International Conference of the IEEE Engineering in Medicine and Biology Society (2012) 6665–6668, http://dx.doi.org/10.1109/EMBC.2012.6347523.

[21] V.G. Eck, W.P. Donders, J. Sturdy, J. Feinberg, T. Delhaas, L.R. Hellevik, W. Huberts, A guide to uncertainty quantification and sensitivity analysis for cardiovascular applications, Int. J. Numer. Methods Biomed. Eng. (2015), http://dx.doi.org/10.1002/cnm.2755.

[22] I. Sobol, Global sensitivity indices for nonlinear mathematical models and their Monte Carlo estimates, Math. Comput. Simul. 55 (2001) 271–280, http://dx.doi.org/10.1016/S0378-4754(00)00270-6.

[23] A. Saltelli, Global Sensitivity Analysis: The Primer, John Wiley, Chichester, England, 2008.

[24] D. Xiu, G.E.M. Karniadakis, The Wiener-Askey polynomial chaos for stochastic differential equations, SIAM J. Sci. Comput. 24 (2) (2002) 619–644.

[25] J. Feinberg, H.P. Langtangen, Chaospy: an open source tool for designing methods of uncertainty quantification, J. Comput. Sci. 11 (2015) 46–57, http://dx.doi.org/10.1016/j.jocs.2015.08.008.

[26] L. Breiman, Random forests, Mach. Learn. 45 (1) (2001) 5–32, http://dx.doi.org/10.1023/A:1010933404324.

[27] R.E. Caflisch, Monte Carlo and quasi-Monte Carlo methods, Acta Numer. 7 (1998) 1–49, http://dx.doi.org/10.1017/S0962492900002804.

[28] A. Saltelli, Making best use of model evaluations to compute sensitivity indices, Comput. Phys. Commun. 145 (2) (2002) 280–297, http://dx.doi.org/10.1016/S0010-4655(02)00280-1.

[29] J. Friedman, T. Hastie, R. Tibshirani, The Elements of Statistical Learning, vol. 1, Springer Series in Statistics Springer, Berlin, 2001.

[30] C.B. Storlie, L.P. Swiler, J.C. Helton, C.J. Sallaberry, Implementation and evaluation of nonparametric regression procedures for sensitivity analysis of computationally demanding models, Reliab. Eng. Syst. Saf. 94 (11) (2009) 1735–1763, http://dx.doi.org/10.1016/j.ress.2009.05.007.

[31] H. Sathyanarayanamurthy, R.B. Chinnam, Metamodels for variable importance decomposition with applications to probabilistic engineering design, Comput. Ind. Eng. 57 (3) (2009) 996–1007, http://dx.doi.org/10.1016/j.cie.2009.04.003.

[32] A. Gelman, J. Hill, Data Analysis Using Regression and Multilevel/Hierarchical Models. Analytical Methods for Social Research, Cambridge University Press, Cambridge; New York, 2007, oCLC: ocm67375137.

[33] J. Salvatier, T.V. Wiecki, C. Fonnesbeck, Probabilistic programming in Python using PyMC3, PeerJ Comput. Sci. 2 (2016) e55, http://dx.doi.org/10.7717/peerj-cs.55.

[34] S.N. Hunyor, J.M. Flynn, C. Cochineas, Comparison of performance of various sphygmomanometers with intra-arterial blood-pressure readings, Br. Med. J. 2 (6131) (1978) 159–162.

[35] G. Rogers, T. Oosthuyse, A comparison of the indirect estimate of mean arterial pressure calculated by the conventional equation and calculated to compensate for a change in heart rate, Int. J. Sports Med. 21 (02) (2000) 90–95, http://dx.doi.org/10.1055/s-2000-8865.

[36] J. Pugsley, A.B. Lerner, Cardiac output monitoring: is there a gold standard and how do the newer technologies compare? Semin. Cardiothorac. Vasc. Anesth. 14 (4) (2010) 274–282, http://dx.doi.org/10.1177/1089253210386386.

[37] M. Chakravarthy, Cardiac output – have we found the 'gold standard'? Ann. Cardiac Anaesth. 11 (1) (2008) 1, http://dx.doi.org/10.4103/0971-9784.38441.

[38] S. Meyer, D. Todd, I. Wright, L. Gortner, G. Reynolds, Review article: non-invasive assessment of cardiac output with portable continuous-wave Doppler ultrasound, Emerg. Med. Australasia 20 (3) (2008) 201–208, http://dx.doi.org/10.1111/j.1742-6723.2008.01078.x.

[39] H.L. Tan, M. Pinder, R. Parsons, B. Roberts, P.V. van Heerden, Clinical evaluation of USCOM ultrasonic cardiac output monitor in cardiac surgical patients in intensive care unit, Br. J. Anaesth. 94 (3) (2005) 287–291, http://dx.doi.org/10.1093/bja/aei054.

[40] R. Chand, Y. Mehta, N. Trehan, Cardiac output estimation with a new Doppler device after off-pump coronary artery bypass surgery, J. Cardiothorac. Vasc. Anesth. 20 (3) (2006) 315–319, http://dx.doi.org/10.1053/j.jvca.2005.05.024.

[41] T.M. Chou, K. Sudhir, S. Iwanaga, K. Chatterjee, P.G. Yock, Measurement of volumetric coronary blood flow by simultaneous intravascular two-dimensional and Doppler ultrasound: validation in an animal model, Am. Heart J. 128 (2) (1994) 237–243, http://dx.doi.org/10.1016/0002-8703(94)90474-X.

[42] N.H. Pijls, B. de Bruyne, Coronary Pressure, Springer Science & Business Media, 2013.

[43] S. Sankaran, H.J. Kim, G. Choi, C.A. Taylor, Uncertainty quantification in coronary blood flow simulations: impact of geometry, boundary conditions and blood viscosity, J. Biomech. 49 (12) (2016) 2540–2547, http://dx.doi.org/10.1016/j.jbiomech.2016.01.002.

[44] T. Kenner, The measurement of blood density and its meaning, Basic Res. Cardiol. 84 (2) (1989) 111–124, http://dx.doi.org/10.1007/BF01907921.

[45] N. Suwa, T. Niwa, H. Fukasawa, Y. Sasaki, Estimation of intravascular blood pressure gradient by mathematical analysis of arterial casts, Tohoku J. Exp. Med. 79 (2) (1963) 168–198, http://dx.doi.org/10.1620/tjem.79.168.

[46] A. Saltelli, P. Annoni, I. Azzini, F. Campolongo, M. Ratto, S. Tarantola, Variance based sensitivity analysis of model output. Design and estimator for the total sensitivity index, Comput. Phys. Commun. 181 (2) (2010) 259–270, http://dx.doi.org/10.1016/j.cpc.2009.09.018.

[47] T.G. Flohr, R. Raupach, H. Bruder, Cardiac CT: how much can temporal resolution, spatial resolution, and volume coverage be improved? J. Cardiovasc. Comput. Tomogr. 3 (3) (2009) 143–152, http://dx.doi.org/10.1016/j.jcct.2009.04.004.

[48] S. Abbara, P. Blanke, C.D. Maroules, M. Cheezum, A.D. Choi, B.K. Han, M. Marwan, C. Naoum, B.L. Norgaard, R. Rubinshtein, P. Schoenhagen, T. Villines, J. Leipsic, SCCT guidelines for the performance and acquisition of coronary computed tomographic angiography: A report of the Society of Cardiovascular Computed Tomography Guidelines Committee: endorsed by the North American Society for Cardiovascular Imaging (NASCI), J. Cardiovasc. Comput. Tomogr. 10 (6) (2016) 435–449, http://dx.doi.org/10.1016/j.jcct.2016.10.002.

[49] S. Kishi, A.A. Giannopoulos, A. Tang, N. Kato, Y.S. Chatzizisis, C. Dennie, Y. Horiuchi, K. Tanabe, J.A.A.C. Lima, F.J. Rybicki, D. Mitsouras, Fractional flow reserve estimated at coronary ct angiography in intermediate lesions: comparison of diagnostic accuracy of different methods to determine

coronary flow distribution, Radiology 287 (1) (2018) 76–84, http://dx.doi.org/10.1148/radiol.2017162620.
[50] I. Decramer, P.K. Vanhoenacker, G. Sarno, L. Van Hoe, O. Bladt, W. Wijns, P.M. Parizel, Effects of sublingual nitroglycerin on coronary lumen diameter and number of visualized septal branches on 64-MDCT angiography, Am. J. Roentgenol. 190 (1) (2008) 219–225, http://dx.doi.org/10.2214/AJR.07.2648.
[51] K. Hirohata, A. Kano, A. Goryu, J. Ooga, T. Hongo, S. Higashi, Y. Fujisawa, S. Wakai, K. Arakita, Y. Ikeda, S. Kaminaga, B.S. Ko, S.K. Seneviratne, A novel CT-FFR method for the coronary artery based on 4D-CT image analysis and structural and fluid analysis, in: Medical Imaging 2015: Physics of Medical Imaging, International Society for Optics and Photonics, 2015, pp. 94122O, http://dx.doi.org/10.1117/12.2081674.
[52] O. Wever-Pinzon, J. Romero, I. Kelesidis, J. Wever-Pinzon, C. Manrique, D. Budge, S.G. Drakos, I.L. Pi na, A.G. Kfoury, M.J. Garcia, J. Stehlik, Coronary computed tomography angiography for the detection of cardiac allograft vasculopathy, J. Am. Coll. Cardiol. 63 (19) (2014) 1992–2004, http://dx.doi.org/10.1016/j.jacc.2014.01.071.
[53] R. Wang, S. Baumann, U.J. Schoepf, F.G. Meinel, J.D. Rier, J.Z. Morris, H. Möllmann, C.W. Hamm, D.H. Steinberg, M. Renker, Comparison of quantitative stenosis characteristics at routine coronary computed tomography angiography with invasive fractional flow reserve for assessing lesion-specific ischemia, J. Cardiovasc. Comput. Tomogr. 9 (6) (2015) 546–552, http://dx.doi.org/10.1016/j.jcct.2015.08.003.
[54] B.L. Nørgaard, J.M. Jensen, J. Leipsic, Fractional flow reserve derived from coronary CT angiography in stable coronary disease: a new standard in non-invasive testing? Eur. Radiol. 25 (8) (2015) 2282–2290, http://dx.doi.org/10.1007/s00330-015-3619-1.
[55] S. Achenbach, Computed tomography coronary angiography, J. Am. Coll. Cardiol. 48 (10) (2006) 1919–1928, http://dx.doi.org/10.1016/j.jacc.2006.08.012.
[56] C. Collet, Y. Onuma, M. Grundeken, Y. Miyazaki, M. Bittercourt, P. Kitslaar, S. Motoyama, Y. Ozaki, T. Asano, J. Wentzel, G. Streekstra, P. Serruys, R. de Winter, R. Planken, In vitro validation of coronary CT angiography for the evaluation of complex lesions, EuroIntervention 13 (15) (2018) e1823–e1830, http://dx.doi.org/10.4244/EIJ-D-17-00326.
[57] K. Uzu, H. Otake, G. Choi, T. Toba, H.J. Kim, A. Roy, M. Schaap, L. Grady, M. Kawata, T. Shinke, C.A. Taylor, K.-I. Hirata, Lumen boundaries extracted from coronary computed tomography angiography on computed fractional flow reserve (FFRCT): validation with optical coherence tomography, EuroIntervention (2018), http://dx.doi.org/10.4244/EIJ-D-17-01132.
[58] H.Y. Kim, H.-S. Lim, J.-H. Doh, C.-W. Nam, E.-S. Shin, B.-K. Koo, M.-H. Yoon, S.-J. Tahk, D.K. Kang, Y.B. Song, J.-Y. Hahn, S.H. Choi, H.-C. Gwon, S.-H. Lee, E.-K. Kim, S.M. Kim, Y. Choe, J.-H. Choi, Physiological severity of coronary artery stenosis depends on the amount of myocardial mass subtended by the coronary artery, JACC: Cardiovasc. Interv. 9 (15) (2016) 1548–1560, http://dx.doi.org/10.1016/j.jcin.2016.04.008.
[59] A.H. Waller, R. Blankstein, R.Y. Kwong, M.F. Di Carli, Myocardial blood flow quantification for evaluation of coronary artery disease by positron emission tomography, cardiac magnetic resonance imaging, and computed tomography, Curr. Cardiol. Rep. 16 (5) (2014) 483, http://dx.doi.org/10.1007/s11886-014-0483-6.
[60] H. Fukasawa, Hemodynamical studies of cerebral arteries by means of mathematical analysis of arterial casts, Tohoku J. Exp. Med. 99 (3) (1969) 255–268, http://dx.doi.org/10.1620/tjem.99.255.
[61] G.M. Hutchins, M.M. Miner, J.K. Boitnott, Vessel caliber and branch-angle of human coronary artery branch-points, Circ. Res. 38 (6) (1976) 572–576.
[62] M.A. Changizi, C. Cherniak, Modeling the large-scale geometry of human coronary arteries, Can. J. Physiol. Pharmacol. 78 (8) (2000) 603–611.
[63] R. Revellin, F. Rousset, D. Baud, J. Bonjour, Extension of Murray's law using a non-Newtonian model of blood flow, Theor. Biol. Med. Model. 6 (2009) 7, http://dx.doi.org/10.1186/1742-4682-6-7.
[64] H.A. Kirişli, M. Schaap, C.T. Metz, A.S. Dharampal, W.B. Meijboom, S.L. Papadopoulou, A. Dedic, K. Nieman, M.A. de Graaf, M.F.L. Meijs, M.J. Cramer, A. Broersen, S. Cetin, A. Eslami, L. Flórez-Valencia, K.L. Lor, B. Matuszewski, I. Melki, B. Mohr, I. Öksüz, R. Shahzad, C. Wang, P.H. Kitslaar, G. Unal, A. Katouzian, M. Orkisz, C.M. Chen, F. Precioso, L. Najman, S. Masood, D. Ünay, L. van Vliet, R. Moreno, R. Goldenberg, E. Vuç ini, G.P. Krestin, W.J. Niessen, T. van Walsum, Standardized evaluation framework for evaluating coronary artery stenosis detection, stenosis quantification and lumen segmentation algorithms in computed tomography angiography, Med. Image Anal. 17 (8) (2013) 859–876, http://dx.doi.org/10.1016/j.media.2013.05.007.
[65] Y. He, D. Xiu, Numerical strategy for model correction using physical constraints, J. Comput. Phys. 313 (2016) 617–634, http://dx.doi.org/10.1016/j.jcp.2016.02.054.